Available online at www.sciencedirect.com
SCIENCE DIRECT®
Journal of Power Sources 136 (2004) 88–98
JOURNAL OF POWER SOURCES
www.elsevier.com/locate/jpowsour

Improvement of the cycleability of nano-crystalline lithium manganate cathodes by cation co-doping

S. Nieto, S.B. Majumder, R.S. Katiyar*

Department of Physics, University of Puerto Rico, San Juan, PR 00923-3343, USA

Received 2 April 2004; accepted 3 May 2004

Available online 4 July 2004

Abstract

Lithium manganate spinel is extensively studied as a positive electrode in lithium ion rechargeable batteries. Growth of nano-size cathode particles is proposed to improve the rate capabilities of these cathode materials. It remains controversial if the particle size in the nano-range (as compared to the conventional micrometer size particles of these materials) has any appreciable influence on the discharge capacity, rate capabilities, and cycleability of these materials. In the 4 V range, especially at slightly elevated temperature, lithium manganate exhibits capacity fading though the underlying mechanism for such fading is not yet clear. In the present work, we have successfully prepared nano-crystalline lithium manganate spinel powder by an acetate base solution route. Though the discharge capacity of these nano-crystalline cathodes was equivalent to their microcrystalline counterpart, these exhibited capacity fading in the 4 V range. Through a combined X-ray diffraction, micro-Raman spectroscopy, and X-ray photoelectron spectroscopy (XPS) analyses, we correlated the observed capacity fading with the onset of Jahn–Teller (J–T) distortion toward the end of the discharge in the cut-off limit between 4.2 and 3.4 V. It was postulated that if J–T distortion is the dominant fading mechanism of these nano-crystalline cathodes then by increasing the average oxidation state of the Mn ions in a virgin lithium manganate cathode, the onset of such distortion towards the end of the discharge could be delayed, and therefore, the cycleability of these cathodes could be improved. By synthesizing lithium and aluminum ion co-doped lithium manganate particles, we could increase the average oxidation state of the Mn ions in the virgin electrodes. Indeed, the cycleability of these co-doped cathodes was dramatically improved which supports our postulation. The doping contents of lithium and aluminum, however, should be further optimized to further increase the discharge capacity of these modified cathodes.

Keywords: Nano-crystalline lithium manganate; Li ion battery; Electrochemical properties; Doping

1. Introduction

Li ion rechargeable batteries have better performance over the other competitive rechargeable batteries due to their higher operative voltage (around 3–4 V range), high-energy storage capacity, low self-discharge, and high cycleability. For the application in high power devices (viz. devices for telecommunication, various consumer electronic products such as laptop, camcorder, etc.), the discharge capacity of Li ion batteries at higher current rate required is to be improved. As diffusion of lithium ions inside the active material particles is the rate-limiting step of intercalation process, faster Li^+ diffusion in the electrode materials could improve the rate capabilities of Li ion batteries. In this regard, development of nano-structured electrodes is attractive, since in such electrodes, Li^+ diffusion distance is dramatically reduced and faster Li^+ diffusion yields better electrochemical performance of the electrode materials. Thus it is reported that nano-crystalline ferric oxide exhibits very high lithium intercalation capacity, excellent rate capability, and capacity retention [1]. Other nano-crystalline transition metal oxides (CuO, Ni, Co, etc.) as anode material were also reported to have high capacity, excellent capacity retention up to 100 cycles, and high recharging rates [2]. Nano-crystalline Si composite with carbon black has been reported to have shown extremely high reversible capacity ∼1700 mAh/g [3]. Improved Li^+ intercalation behavior in carbon-nanotubes (as anode) has been reported [4]. Aerogels, due to their high specific surface area and interconnected solid network structure, have been shown to exhibit high specific energy [5]. The rate capabilities of a variety of electrode materials were vastly improved by growing them in the form of nano-tubules directly on the current collector surface by a template synthesis technique [6]. Apart from the anode and cathode materials, electrolyte also influences the electrochemical performance

* Corresponding author. Tel.: +1 787 751 4210; fax: +1 787 764 2571.
E-mail address: rkatiyar@rrpac.upr.clu.edu (R.S. Katiyar).

0378-7753/$ – see front matter © 2004 Elsevier B.V. All rights reserved.
doi:10.1016/j.jpowsour.2004.05.020

of Li ion batteries. Conventionally, liquid electrolytes (consisting a Li based salt and carbonate salt mixtures) are used in Li ion based batteries. However, research is underway to make all solid state, flexible Li ion batteries for better performance [7]. Polymer, ceramic oxide nano-powder, composites exhibit promising characteristics as solid state electrolytes. The introduction of nano-crystalline ceramic oxides has been reported to reduce the glass transition temperature of the polymer and thereby increase the Li^+ conductivity at room temperature [8].

Lithium manganate ($Li_{1-x}Mn_2O_4$) (LMO) with cubic spinel structure is considered to be less expensive, environmentally benign alternative material to the conventional layered $LiCoO_2$ based cathodes. In the spinel LMO, Li ions occupy tetrahedral (8a) sites, Mn ions (Mn^{3+}/Mn^{4+}) occupy octahedral (16d) sites, and the O^{2-} ions occupy the octahedral (32e) sites. The oxygen ions form a cubic closed-pack array. The tetrahedral (8a) sites share face with vacant octahedral site (16c), so that eventually 3-dimensional 8a–16c–8a–16c channel is formed for the Li^+ intercalation. In the composition range ($0 \leq x \leq 1$), LMO remains cubic, i.e the electrochemical extraction of lithium from the tetrahedral sites of $LiMn_2O_4$ (~4 V) does not alter the cubic symmetry of the spinel electrode. The electrochemical reaction is represented as

$$LiMn_2O_4 \Leftrightarrow Li_{1-x}Mn_2O_4 + xLi^+ + xe^- \quad (1)$$

The Li^+ extraction/insertion occurs in two-step in the composition range $0 \leq x \leq 0.5$ and $0.5 \leq x \leq 1.0$, respectively. However, the crystal structure always remain cubic. In the composition range $1.0 \leq x \leq 2.0$ the cubic spinel phase (lattice parameter, $a = 8.248$ Å) transforms to a tetragonal rock-salt phase ($a = 8.007$ Å, c = 9.274 Å) at ~3 V.

$$Li + LiMn_2O_4 \Leftrightarrow Li_2Mn_2O_4 \quad (2)$$

The cubic to tetragonal phase transition is associated with 16% increase of the *c*/*a* ratio of the unit cell. Cycling in 3 V range often reported to have poor capacity retention of the battery as the large anisotropic change in the lattice parameter are too severe for the cathode particle to maintain their structural integrity with the current collector. Even in the 4 V range, poor rate capabilities (especially when discharged at high load current), capacity fading (particularly at elevated temperatures), and self discharge of LMO based cathodes remain some of the major hindrance factors for their use in commercial devices [9].

Since the nano-particles have large surface area to volume ratio, the effective charge transfer should be superior, and accordingly, it was demonstrated the intercalation of alkali metals nano-crystalline materials were better [10]. Extensive investigations on the LMO cathode were performed using micrometer size particles and their electrochemical properties were optimized for practical applications. Recently, several research efforts are made to synthesize nano-crystalline LMO particles and study their electrochemical properties. Some of the reported electrochemical

Table 1
Electrochemical properties of nano-crystalline $LiMn_2O_4$ cathode

Synthesis route	Particle size	Discharge capacity (mAh/g)	Capacity retained upon cycling	Predicted mechanism for capacity fading	Reference
Sol–gel	5–108 nm, particle size increased with the increase of the calcination temperature from 350 to 650 °C	Increased from 83 to 117 (4 V range) and from 76 to 110 (3 V range) with the increase in particle size	Decreased from 80 to 67% (50 cycles) (4 V) and from 45 to 10% (3 V) with the increase in particle size	At 4 V range, fading due to lattice strain associated with cubic–cubic structural transition and at 3 V range, fading due to J–T distortion	[11]
Hydroxide based solution route	$LiMn_{1.97}Li_{0.03}O_4$, 500 nm	129 (4 V)	91.9% (50 cycles), at C/5 rate	Improved fading due to suppression of cubic–cubic structural transition	[12]
Sonolysis	60–100 nm	150 in the first discharge, 70 in the second discharge	Severe capacity fading	Capacity fading due to poor electrical contact of the nano-crystalline active materials with current collector	[13]
Acetate based solution route	Particle size not mentioned	120 (4 V); load current, 0.1 mA/cm^2	75% retention (55 cycles)	Fading is dominated by Mn dissolution	[14]
Mechano-chemical synthesis	9.7 nm (ball-milled, without calcination), 214 nm (ball-milled followed by calcination)	167 (4.3–2.4 V) for 10 nm particle, 214 (4.2–2.4 V) for 841 nm particles	72% (for 10 nm particle), 36% (for 814 nm particle at C/3 rate) after 11 cycles	Finer particles suppress the J–T distortion and fading is improved	[15]
Nitrate based solution route	50–100 nm	55–130 (4 V range, 11–0.4 mA/cm^2 load current)	80% retention (140 cycles), at 0.4 mA/cm^2 load current	Fading due to Mn dissolution	[16]
Solid state reaction followed by ball-milling	Aggregates of nano-crystallites to form larger particles	130 (3 V), load current 0.5 A/cm^2	No capacity fading	Nano-crystallites in larger particles minimize J–T distortion	[17]

properties of nano-crystalline LMO are summarized in Table 1. As shown in the table, from these studies, it is not very clear whether the use of nano-crystalline LMO cathode would have any beneficiary effect over their micron size counterpart or not. Moreover, the underlying mechanism control the capacity fading both at 4 and 3 V range is not well understood [11–17]. Possibly the kinetics of the intercalation behavior of Li^+ ions in nano-crystalline LMO are intrinsically different as compared to their micro-crystalline counterpart. Therefore, nano-crystalline materials are required to be further investigated to understand their electrochemical properties in terms of their discharge capacity, charge–discharge behavior and cycleability.

In the present work, we have prepared nano-crystalline LMO powders (particle size < 100 nm) using a cost effective solution growth technique. The phase formation behavior of these powders was characterized by X-ray diffraction. The lattice parameter, crystallite size, and lattice strain were calculated from the slow scanned X-ray diffractograms. The surface morphology of the particles was characterized by transmission as well as scanning electron microscopy. The excellent Li^+ intercalation into the cathode materials was confirmed by cyclic voltammetry. In the voltage range between 4.2 and 3.4 V and between 4.2 and 2.6 V, the LMO cathode had a discharge capacity ∼118 and 220 mAh/g, respectively. These cathodes, however, exhibited severe capacity fading in the 4 V range. On the basis of XPS analyses in conjunction with XRD and micro-Raman spectroscopy measurements, we have argued that the capacity fading is due to the early onset of Jahn–Teller (J–T) distortion during the repeated charge–discharge cycles. LMO films co-doped with Li and Al were found to be effective to reduce the early onset of J–T distortion (>3 V regime) and thereby improve the cycleability of nano-crystalline LMO.

2. Experimental

Lithium manganate powder was synthesized by chemical solution route using lithium acetate and manganese acetate as precursor materials. The details of the powder synthesis have been reported elsewhere [18]. Aluminum nitrate was used as precursor material to prepare Al doped lithium manganate composition. The phase formation behavior of the calcined powder was characterized by XRD using Cu Kα radiation in the 2θ ranges of 15–70°. Selected diffraction peaks were slow scanned at a scanning speed of $0.3^\circ\ min^{-1}$. From the recorded XRD pattern, the accurate peak position (2θ) as well as the full-width at half maxima (FWHM) (β) of each slow scanned diffraction peaks was estimated by fitting the diffraction peak with Pearson VII amplitude function using a commercial peak fit software. These values were used to calculate the crystallite size and lattice strain of the synthesized powder using Williamson Hall equation [19]. X-ray photoelectron spectroscopy (XPS) measurements were performed by a PHI5600 ESCA system (Physical Electronics), using Al Kα radiation. Curve fitting of the slow scanned XPS spectra was carried out using a non-linear least squares fitting program with a Gaussian–Lorentzian sum function. All binding energies reported in this paper were charge-corrected using the C 1s peak (284.5 eV) from the C black in the composite electrode. Raman measurements were performed using a Jobin–Yvon T64000 spectrophotometer consisting a double premonochromator coupled to a third monochromator/spectrograph with 1800 grooves/mm grating. The 514.5 nm radiation of an Ar^+ laser was focused in a less than 2 μm diameter circle area by using Raman micro-probe with an 80× objective. The same microscope was used to collect the signal in backscattering geometry and to focus it at the entrance of the premonochromator. The scattered light, dispersed by the spectrophotometer was detected by a charge coupled device detection system.

The electrochemical characteristics of the nano-crystalline powders were carried out in a two-electrode test cell kept inside a glove box. A composite electrode consisting of nano-size LMO powder, carbon black, and the polyvinylidene binder in the weight ratio of 80:10:10 was used as the working electrode. Lithium metal foils were used as the counter and reference electrodes. $LiPF_6$ (1 M) in a 1:1 (by weight) mixture of ethylene carbonate and dimethyl carbonate (DMC) was used as electrolyte. Celgard 2400 was used as separator between anode and cathode. A computer controlled potentiostat/galvanostat system [consisting a PC 750.4 controller and PHE 200 software (Gamry Instruments)] was used for cyclic voltammetry and charge–discharge measurements. The CV plots were recorded at a scan speed of $0.2\ mV\ s^{-1}$ in a voltage range of 4.2–3.4 V, unless mentioned otherwise. Charge–discharge measurements at ambient temperature were performed in a voltage range of 4.2–3.4 V (unless specified otherwise) at 0.98 C rates.

3. Results and discussions

Stoichiometric lithium manganate ($LiMn_2O_4$) (LMO) powders were calcined in the temperature range of 600–850 °C for extended period ranging from 1 to 24 h. At relatively lower temperature (≤700 °C), the annealing for 2 h yielded cubic spinel phase mixed with small amount of Mn_2O_3. However, phase pure LMO spinel was obtained up on calcining the powders either for extended time or at higher calcination temperature ∼800 °C.

Fig. 1(a) shows the transmission electron micrograph (TEM) of solution synthesized spinel $LiMn_2O_4$ powder calcined at 700 °C for 15 h. Within the selected region for TEM observation, particles in the size range of 60–100 nm are visible. In some regions agglomerates are also identified. A separated particle is shown in Fig. 1(b). The black contours inside the grain (marked by arrow) are believed to be due to retained strain (see the XRD analyses reported

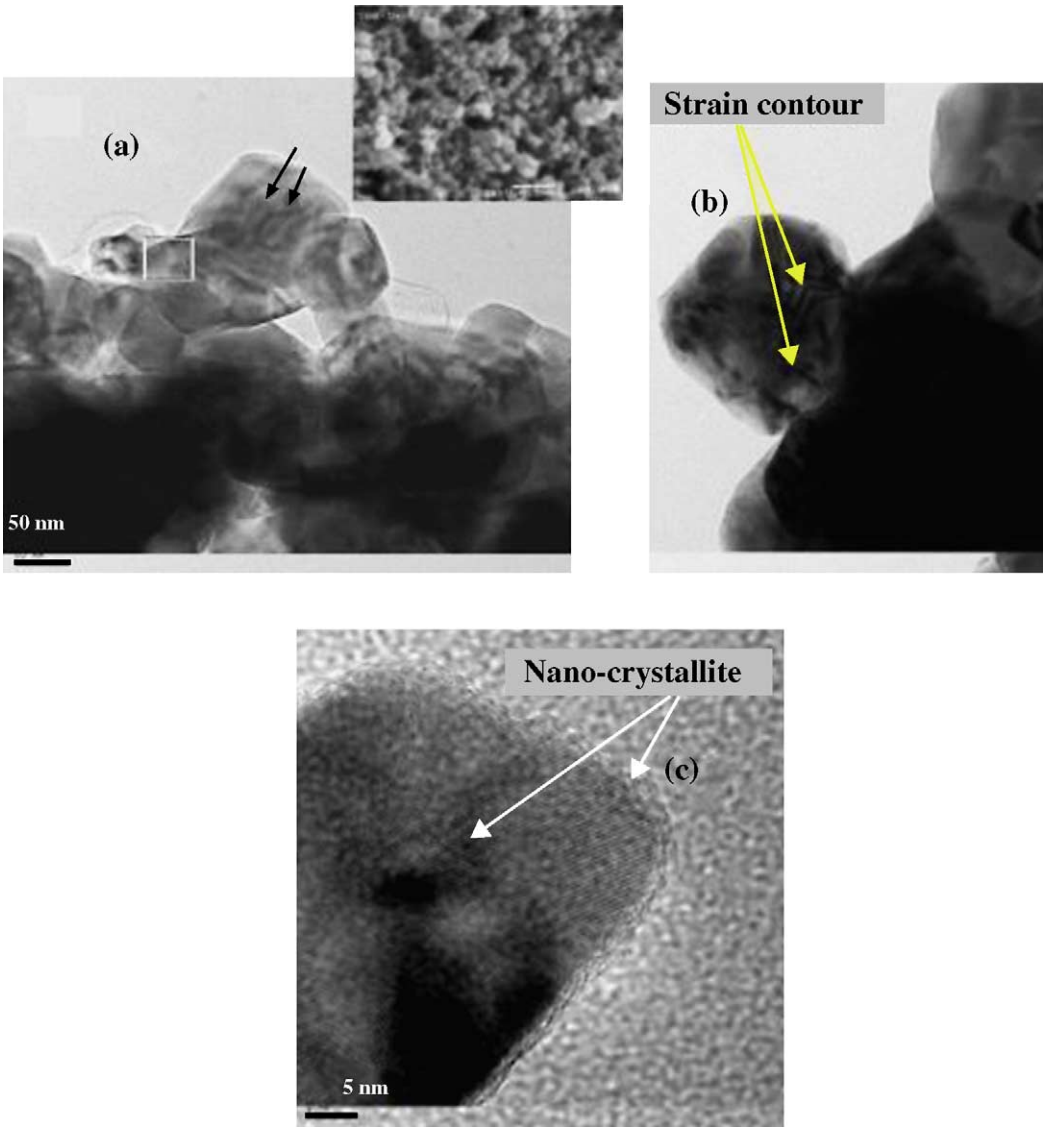

Fig. 1. (a) TEM micrographs of calcined lithium manganate powders. The inset shows the SEM micrograph of the composite lithium manganate cathode. (b) TEM micrograph of a single lithium manganate particle and (c) the high resolution TEM micrograph of a single lithium manganate shows that each particle is the aggregates of several nano-crystallites.

later). Close inspection of Fig. 1(b) shows that each single particle consists of several nano-crystallites. Fig. 1(c) shows the magnified TEM micrograph of such an individual particle. It is clearly seen that the particle constitutes several nano-crystallite having lattice plain oriented in different directions. Similar observation has also been reported in case of solid state prepared $LiMn_2O_4$ particle ball-milled for extended period of time [17]. The exact mechanism of the formation of such nano-grains either in the solution derived or in extended ball-milled powder so far is poorly understood. Since grown by a solid state route, these particles had larger size as compared to our solution synthesized particles, however, due to the presence of nano-size sub-grains inside the relatively larger particles, the capacity fading due to Jahn–Teller distortion in the 3 V range is reported to be improved.

The nano-powders, synthesized in our laboratory, were tested in terms of their electrochemical characteristics. Fig. 2 shows the typical charge and discharge profile of the assembled cell (composite cathode–liquid electrolyte–anode) in the voltage range between 4.2 and 3.4 V at 0.98 C rate (1 C corresponds to 148 mA/g current to charge/discharge the cell in 1 h). Li ions occupy the tetrahedral 8a sites and the three-dimensional 8a–16c–8a–16c channels provide an energetically favorable pathway for rapid diffusion of Li^+ during charging and discharging. The two plateaus in the 4 V range are due to the ordering of Li^+ in the tetrahedral sites or Mn ions in the octahedral (16d) sites, which corresponds to a cubic-to-cubic transition [20,21]. This two-step extraction (during charging) as well as insertion (during discharging) of Li^+ ions is clearly visible the cyclic voltammograms (CV), where the voltages corresponding the plateau match

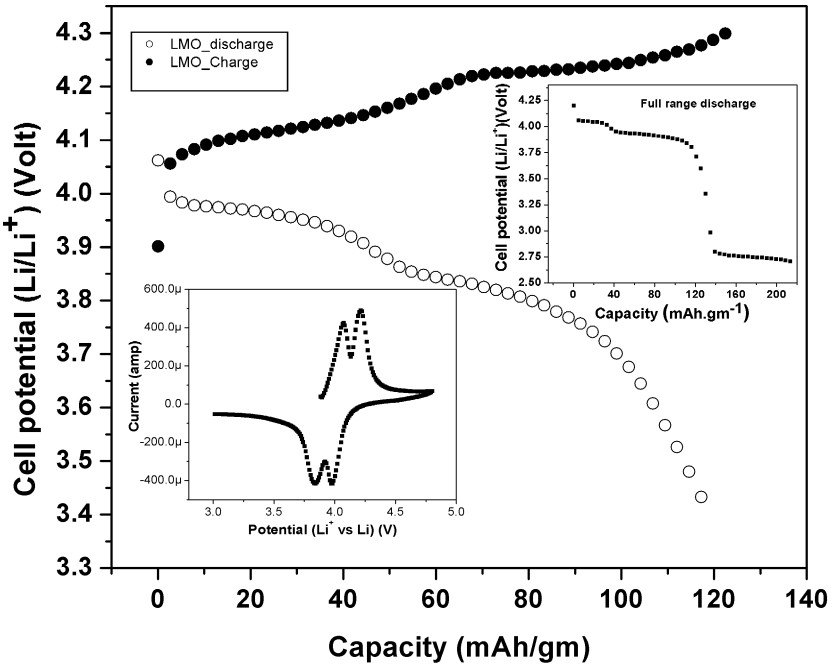

Fig. 2. The discharge capacity of nano-crystalline lithium manganate composite cathode in the 4 V range. The inset shows the cyclic voltammogram in the 4 V range and the discharge capacity in the voltage range of 4.2–2.6 V.

well with the peaks of the CV plot (see inset). During deep discharge (see the other inset), all the available tetrahedral sites are already filled and Li^+ ions are inserted into the octahedral sites about 2.8 V and the material has undergone a cubic to tetragonal structural transition with a 6.5% volume expansion (Jahn–Teller distortion) [22]. For the present work, we have concentrated on the charge–discharge characteristics in the 4.2–3.4 V (4 V range) regime where apparently, the J–T distortion should not affect the cycleability of the cathode materials. The charge–discharge characteristics of the synthesized nano-materials, both in the 4 and 3 V ranges, are better or comparable [11–17] with the existing literature reports. However, severe capacity fading was observed when these nano-crystalline LMO cathodes were repeatedly cycled galvanostatically in the 4 V range, at ~1 C rate. As, for example, within five charge–discharge cycles, the capacity dropped from 120 down to 72 mAh/g. To gain better insight about the observed capacity fading, the characteristic (1 1 1), (3 1 1), (4 0 0), and (4 4 0) slow scanned X-ray diffraction (XRD) peaks of spinel LMO were recorded from as prepared as well as 25 times cycled electrodes. Fig. 3 shows the (4 4 0) peak before and after charge–discharge cycling. As compared to the virgin electrode, the full-width half maxima (FWHM) of (4 4 0) peak is significantly increased after cycling. Similar features were also observed in the other diffraction peaks. To obtain accurate peak position (2Θ) as well as FWHM values (β) these peaks were fitted to Pearson VII amplitude function using a commercial Peakfit-4 program. After correcting the instrumental broadening [23], the remaining line broadening (β) is believed to be due to the crystallite size (β_{cryst}) and retained strain (β_{strain}) broadening [19]. Therefore,

$$\beta = \beta_{cryst} + \beta_{strain} \tag{3}$$

Now, from Scherrer's equation [23] $\beta_{cryst} = 0.9\lambda_{X\text{-}ray}/t\cos\theta$ (where $\lambda_{X\text{-}ray} = 1.5418$ Å, t is the crystallite size, and θ is the Bragg's diffraction angle) and $\beta_{strain} = 4\epsilon\tan\theta$ [19]. Multiplying both sides of Eq. (1) $\cos\theta/\lambda_{X\text{-}ray}$ and subsequent rearrangement

$$\frac{\beta\cos\theta}{\lambda_{X\text{-}ray}} = \frac{0.9}{t} + \frac{4\varepsilon\sin\theta}{\lambda_{X\text{-}ray}} \tag{4}$$

The intercept and slope of the linear fit of $\beta\cos\theta/\lambda_{X\text{-}ray}$ versus $\sin\theta/\lambda$ plot was used to estimate the crystallite size and lattice strain, respectively. The inset of Fig. 3 shows such linear fit of virgin and after 25 times charged–discharged LMO electrodes. Note that both the crystallite size (t) and lattice strain (ε) are increased after cycling. Marginal increment of the lattice parameter of LMO (8.19 Å) has been observed after 25 cycles (8.20 Å).

It is well known that the nature of an electrode surface is critical for the electrochemical functionality of the material [24]. The surface of the LMO cathode before and after charge–discharge cycle was analyzed by X-ray photoelectron spectroscopy. Fig. 4 shows the slow scanned Mn3p peak of (a) virgin and (b) cycled LMO electrodes. The peaks were deconvoluted using Gaussian–Lorentzian amplitude functions and the fitting parameters are tabulated in Table 2. The Mn3p peak in the binding energy ~49.8 to 50.2 eV and ~48.2 to 48.5 eV is assigned to be due to Mn^{4+} and Mn^{3+} ions, respectively [24]. The integrated area under these fitted peaks denotes the fraction of each of these ion content in the

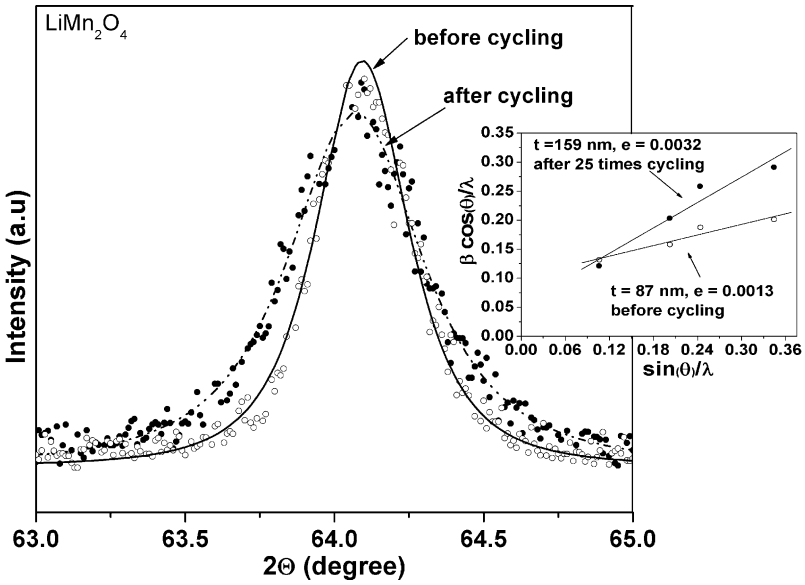

Fig. 3. The experimental (symbol) and fitted (line) slow scanned XRD plot of (4 4 0) diffraction peak of lithium manganate before and after cycling. The inset shows the linear fit of $\beta \cos\theta/\lambda$ vs. $\sin\theta/\lambda$ plot to calculate the crystallite size (intercept) and lattice strain (slope) before and after cycling (see text).

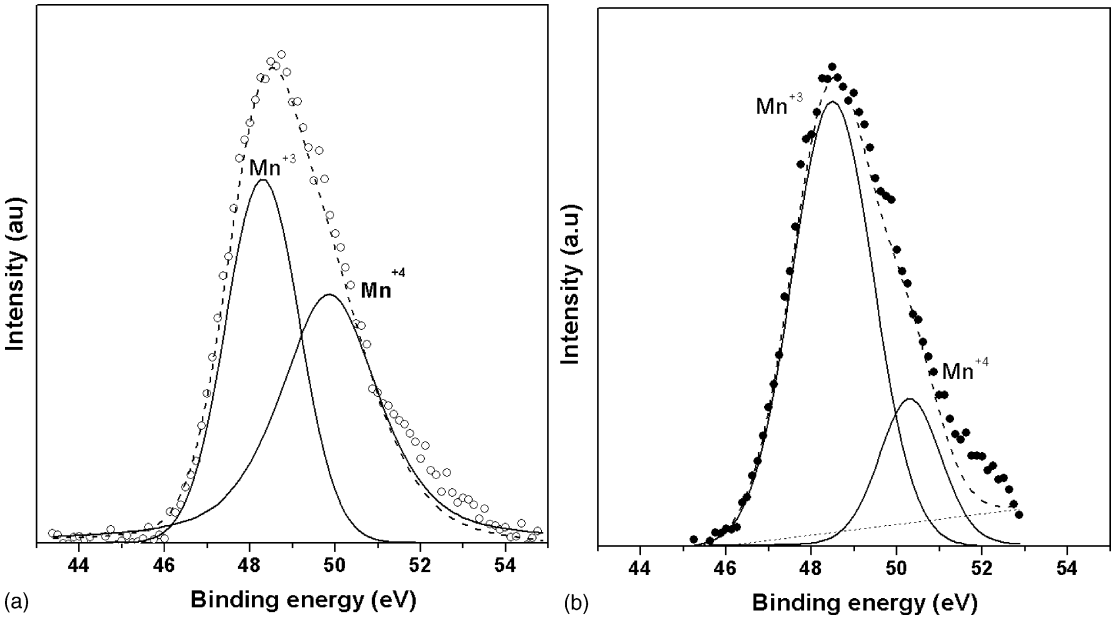

Fig. 4. The slow scanned Mn3p XPS of lithium manganate (a) before and (b) after electrochemical cycling.

Table 2
Summary of the fitting parameters of Mn3p XPS peak of $LiMn_2O_4$ before and after 25th charge–discharge cycles

	Mn3p (eV) [FWHM]	Integral area (sq. unit)	$[Mn^{3+}]$: $[Mn^{4+}]$
Virgin electrode	48.29 [2.03] (Mn^{3+})	2497	0.97:1
	49.86 [2.74] (Mn^{4+})	2583	
After 25th cycles	48.49 [2.23] (Mn^{3+})	4924	3.80:1
	50.31 [1.71] (Mn^{4+})	1296	

cathode material. As shown in Table 2, the ratio of Mn^{3+} and Mn^{4+} ion contents are 0.97:1 for virgin electrode, this is expected since the valence state of Mn ions in stoichiometric $LiMn_2O_4$ should be +3.5, the ratio of Mn should indeed be ∼1:1 as observed. In contrast, after the charge–discharge cycling the Mn^{3+}:Mn^{4+} ratio is drastically increased to 3.80:1. Fig. 5 shows the Raman spectra of (a) virgin and (b) cycled LMO electrode. The assignment of $T_{2g}(1)$, $T_{2g}(2)$, $T_{2g}(3)$, and A_{1g} modes are based on the theoretical calculations on Raman-active modes for $LiMn_2O_4$ reported elsewhere [25]. The T_{2g} (2) as well as T_{2g} (3) phones are characterized by

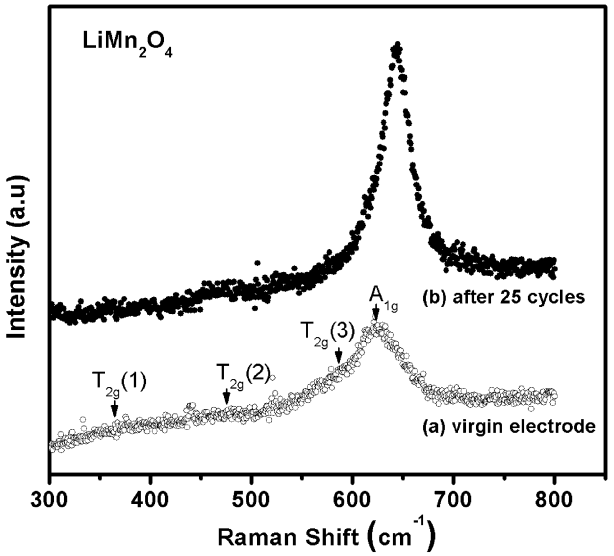

Fig. 5. Micro-Raman spectra of lithium manganate (a) virgin and (b) electrochemically cycled composite cathodes.

large oxygen motions and only marginal Li displacement, whereas T_{2g} (1) phonon vibrations are predominantly due to Li movement in the lattice. A_{1g} mode is also reported to be due to oxygen ion vibration in the lattice. The narrower bandwidth of A_{1g} mode is indicative to symmetric vibration. After cycling, the A_{1g} mode becomes sharper and shifted to higher wave number (Fig. 5(b)). As detected by XPS analysis, the Mn^{3+} ion concentration is dramatically increased after cycling. The ionic radius of Mn^{3+} ion is bigger than Mn^{4+} [26], and therefore, due to the reduction of Mn ions in octahedral 16d site after repeated cycling should indeed shift the A_{1g} phonon mode to higher wave number as observed in the present study. In summary, we have found that after charge–discharge cycling: (i) the Mn^{3+} ion concentration, (ii) the lattice strain, and (iii) crystallite size of nano-crystalline LMO powders are significantly increased where there is marginal increment of the measured lattice parameter.

Although it still remains debatable, the capacity fading of LMO cathode in 4 V range has been attributed to the following three factors namely (i) manganese dissolution into the electrolyte solution [27–31], (ii) J–T distortion due to the formation of tetragonal $Li_2Mn_2O_4$ on LMO surface [32,33], and (iii) development of micro-strain during repeated charge and discharge cycling [9,34]. Most of these studies were performed using solid state prepared LMO with comparatively larger particle size of several micron mean diameter. The nano-crystalline LMO powders exhibited poorer cycleability as compared to their microcrystalline counterpart [16]. It is assumed that for a variety of nano-crystalline cathode materials, efficient electrical contact of the entire active mass to the current collector deteriorates with charge–discharge cycling which results the observed capacity fading [13]. Lucas and Angell [16] relates the capacity fading with the accelerated electrode dissolution in electrolyte due to the larger specific surface area of nano-crystalline LMO powders. Shin and Manthiram [12] on the other hand, observed that even if manganese dissolution is more in chemical solution prepared LMO with smaller particle size (∼1 μm), their cycleability is better as compared to the solid state synthesized larger particles. The better cycleability for the smaller particles were claimed to be related to the suppression of the induced lattice strain during charge–discharge cycles. Thus, the mechanism for capacity fading especially in case of nano-LMO cathodes is so far been poorly understood. Based on our experimental results and the subsequent analyses presented above, we have made an attempt to shed light on the dominant mechanism that leads to poor cycleability of the LMO powders studied in the present work.

Let us first examine if the Mn dissolution into electrolyte solution is the dominant mechanism for capacity fading or not. It is reported that hydrolysis of a fluorinated salt (such as $LiPF_6$ as used in the present study) generates hydrofluoric acid (HF) which in turn dissolve active electrode material from the composite electrode according to the following reaction [14]:

$$2LiMn_2O_4 \Rightarrow 3\lambda MnO_{2_{solid}} + MnO_{solution} + Li_2O_{solution} \quad (5)$$

It has been speculated that the nano-crystalline materials, having larger specific surface area (as compared to their counterpart with larger particle size), would accelerate the dissolution process [14,16]. Electrochemically, it is difficult to extract all the lithium from $LiMn_2O_4$, however, Hunter [35] have demonstrated that by chemical reaction with acid essentially all the Li can be extracted. In practice, as the cell approaches the top of the charge (∼4.2 V), possibly oxygen is lost form LMO lattice ($\sim Li_{1-x}Mn_2O_{4-\sigma}$) lattice which results concomitant reduction of Mn^{4+} to Mn^{3+}. The acid attack eventually drives the following disproportionate reaction at the surface of the electrode material resulting the loss of Mn ions from the lattice [36].

$$2Mn^{3+} \Rightarrow Mn^{4+}_{solid} + Mn^{2+}_{solution} \quad (6)$$

If the dissolution of the active material would the dominant mechanism for the capacity fading in the present case, then the Mn^{4+} ion concentration would have been abundant. On contrary, we have found that after 25th discharge the Mn^{3+} ion concentration is much larger than the Mn^{4+} concentration. The studies on chemically delithiated $Li_{1-x}Mn_2O_4$ also showed that the spinel lattice is not oxygen deficient [37]. Also, as assessed by soaking the electrode in the electrolyte at 55 °C for the extended time [34] or during cycling [9], the degree of manganese dissolution of LMO based electrode was found to be minimal (∼2 wt.%) in $LiMn_2O_4$ and various cation doped $LiMn_{2-y}M_yO_4$ (M = doped cation) cathodes. Therefore, based on our experimental results and the above supportive evidences, the dissolution of active electrode into

the electrolyte solution does not seem to be the dominant mechanism for capacity fading in nano-crystalline materials.

Now let us examine if the onset of J–T distortion towards the end of discharge plays any significant role to the observed capacity fading on nano-crystalline LMO spinel. Under dynamic and non-equilibrium conditions (expedited by high 'C' rate charge/discharge experiments), above 3 V, the onset of Jahn–Teller distortion (cubic to tetragonal structural transition) at the particle surface of the spinel electrode has been reported [32] and also supported by electron diffraction patterns [33,36]. As a result tetragonal $Li_2Mn_2O_4$ was formed on $LiMn_2O_4$ surface at 3.3 V. The mechanism of the formation of $Li_2Mn_2O_4$ has been proposed as follows: during the discharge at lower load current, first all the tetrahedral (8a) sites are filled by Li^+, the voltage then sharply drops to 3 V, and the octahedral (16d) sites start to be filled. On the other hand, when the load current for discharge is higher then the tetrahedral sites are filled normally as long as their availability is high, however, toward the end of the discharge cut-off voltage, when the tetrahedral sites become scarcely available to sustain the current, Li^+ insertion at the octahedral commences (although it is a less energetically favorable alternative) and the cubic spinel transforms to a tetragonal structure. As a result, the valence state of Mn ions in tetragonal structure is reduced to +3 as compared to the valence state of cubic spinel structure (+3.5). Recall our XPS results indicate the appreciable increase of Mn^{3+} concentration after 25th discharge. Therefore, we think that during discharge, tetragonal $Li_2Mn_2O_4$ may indeed have formed at least at the surface of otherwise cubic spinel LMO particles. Since the high spin ionic radius of Mn^{3+} is larger than Mn^{4+}, due to the formation of tetragonal $Li_2Mn_2O_4$ at the surface of cubic spinel particles, the lattice parameter of the cycled electrode is expected to be increased as observed experimentally in the present study. The cubic to tetragonal transition is known to have ~6.5% increase the unit cell volume. In the present study, the increment of lattice strain (due to the lattice mismatch between the two structure) from 0.13% (virgin, cubic spinel) to 0.32% (cycled electrode) (see inset of Fig. 4) probably supports the predicted onset of Jahn–Teller distortion above 3 V regime. The reason behind the appreciable increment of the crystallite size with charge–discharge cycling is not clearly understood; probably, it is also related to the formation of tetragonal $Li_2Mn_2O_4$ on the surface of spinel LMO with cycling. The onset of the J–T distortion and the associated strain in nano-materials may lead to poor electrical contact between the active mass and the current collector and eventually capacity fades with cycling. Alternatively, the induced strain may also distort the 3d 8a–16c–8a–16c pathways for Li^+ diffusion, which results the observed capacity fading.

If the hypothesis of the onset of J–T distortion towards the end of the discharge is indeed the dominant capacity fading mechanism especially in nano-crystalline $LiMn_2O_4$ cathode, then the fading problem should at least be retarded if (i) the average Mn oxidation state in the virgin electrode is increased, as it will delay the J–T onset to lower voltage (below the cut-off potential, 3.2 V); or (ii) increase the Li content in the virgin spinel, so that the delithiated phase does not become unstable and during the discharge at high 'C' rate, Li diffusion at the octahedral site is retarded. To test these hypothesis, a cation co-doping (LMO simultaneously doped with 20 at.% Li and 5.0 at.% Al) approach [12,14] has been adopted to synthesize $Li(Li_{0.20}Al_{0.05}Mn_{1.75})O_4$ (LLAlMO) powder by solution technique. Note that the excess Li^{+1} and Al^{3+} ions presumably replace Mn ions at the

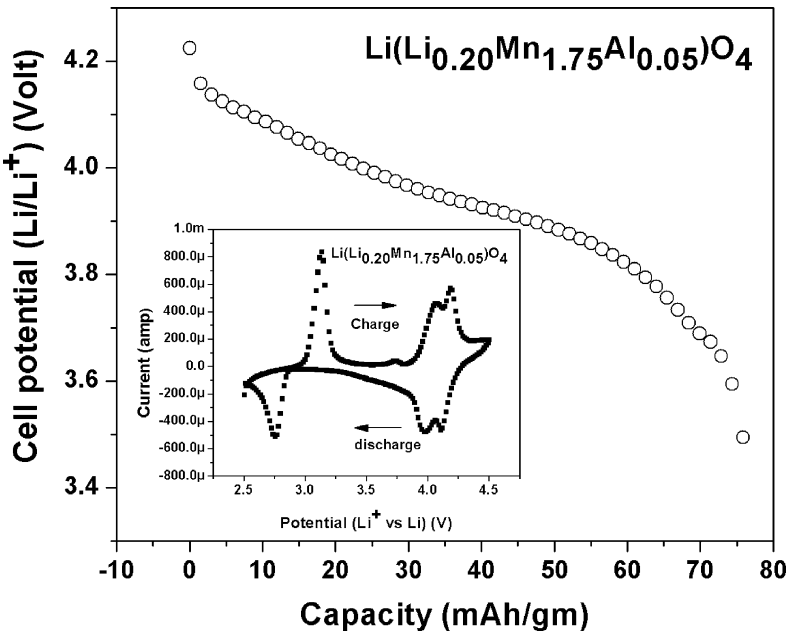

Fig. 6. Discharge capacity of $Li(Li_{0.20}Mn_{1.75}Al_{0.05})O_4$ composite cathode. The inset shows the cyclic voltammogram in the voltage range of 4.5–2.5 V.

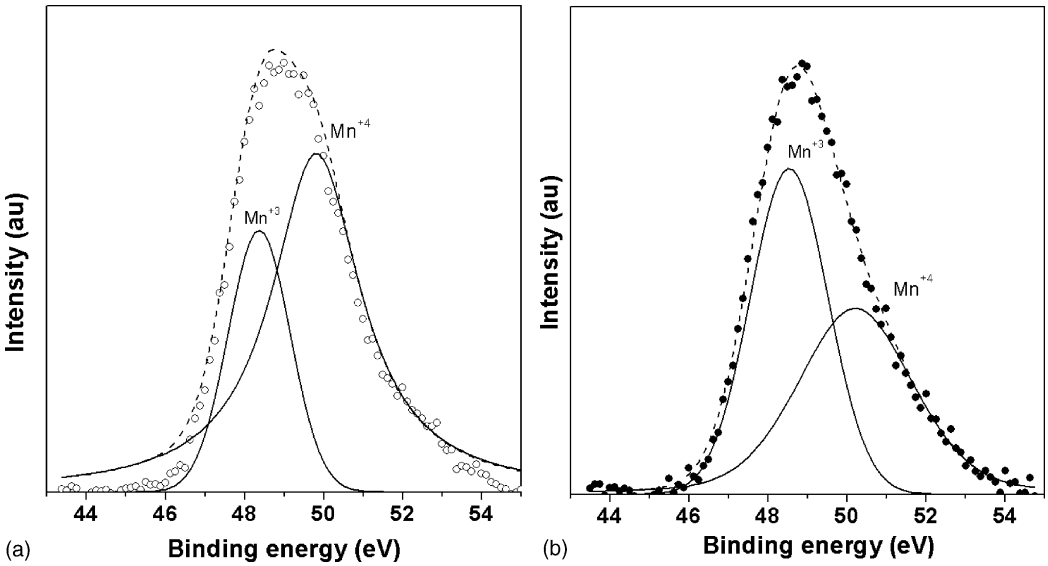

Fig. 7. The slow scanned Mn3p XPS of lithium and aluminum ion co-doped lithium manganate (a) before and (b) after electrochemical cycling.

octahedral site. If we assume that the valence state of Mn ions do not exceed +4 during charging; theoretically, it is predicted that only 0.35 M Li^+ can be extracted from these co-doped material yielding a capacity ~55 mAh/g. The excess Li content and Al doping content can be adjusted to predict capacity that compare close to the unmodified LMO. After charging, 0.85 M Li^+ cannot be extracted from the lattice and it is assumed that 0.65 M remains in the tetrahedral (8a) site and 0.20 M in octahedral (16d) site. As a result of co-substitution, the average valence state of Mn should be raised from +3.5 (stoichiometric cubic spinel) to 3.8 (modified spinel). Fig. 6 shows the typical discharge of LLAlMO powder in the voltage range between 4.2 and 3.4 V. The inset of the figure shows the cyclic voltammogram of the cell in the voltage range of 4.5–2.5 V. The distinct plateau as observed in the discharge profile of pure LMO is not observed in LLAlMO which indicates that the long range cation ordering in the tetrahedral/octahedral sites are disturbed due to the insertion of dopant ion(s). This is also reflected in the CV plot as current peaks in the 4 V range are blurred. The single current peak in the 3 V range corresponds the Li^+ extraction/insertion in octahedral (16d) sites. Fig. 7 shows the slow scanned XPS spectra of Mn3p peak of LLAlMO cathode (a) virgin and (b) after 30th charge and discharge cycle. The fitted parameters are tabulated in Table 3. It is shown that in the virgin electrode, the Mn^{4+} content is indeed increased after co-doping and after electrochemical cycling the Mn^{3+}:Mn^{4+} ratio remains close to 1:1. The structural disorder as well as suppression of Mn^{3+} content is also reflected in the micro-Raman spectra (Fig. 8). The structural disorder is indicated by the disappearance of T_{2g} modes. The shift of A_{1g} mode in LLAlMO virgin electrode towards the lower wave number (~619 cm^{-1} as compared to 623 cm^{-1} in LMO virgin electrode) indicates the abundance of Mn^{4+} ions in the oxygen octahedral cage (Fig. 8(a)). The position of A_{1g} mode remains almost identical (~622 cm^{-1}) after electrochemical cycling indicating the Mn^{3+} content is not significantly increased after cycling (Fig. 8(b)). Fig. 9 shows the slow scanned (4 4 0) diffraction peak of LLAlMO

Table 3
Summary of the fitting parameters of Mn3p XPS peak of $Li(Li_{0.20}Al_{0.05}Mn_{1.75})O_4$ before and after 30th charge–discharge cycles

	Mn3p (eV) [FWHM]	Integral area (sq. unit)	$[Mn^{3+}]$:$[Mn^{4+}]$
Virgin electrode	48.36 [1.85] (Mn^{3+})	2379	0.42:1
	49.81 [2.74] (Mn^{4+})	5730	
After 25th cycles	48.53[2.32] (Mn^{3+})	3295	1.13:1
	50.20 [3.41] (Mn^{4+})	2904	

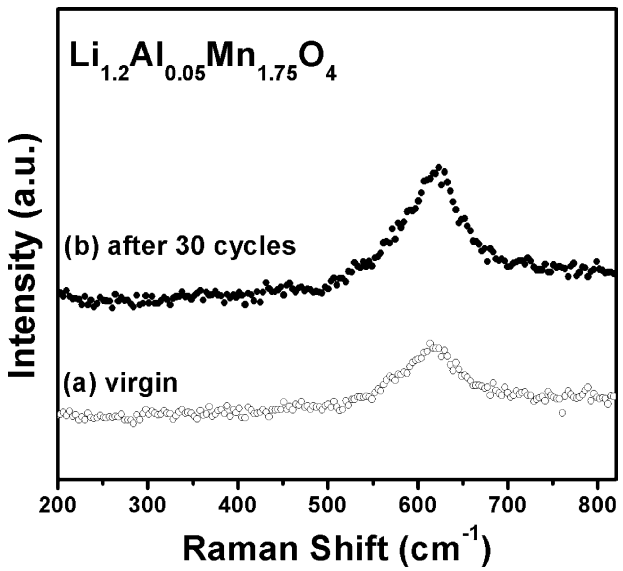

Fig. 8. Micro-Raman spectra of lithium and aluminum ion co-doped lithium manganate: (a) virgin and (b) electrochemically cycled composite cathodes.

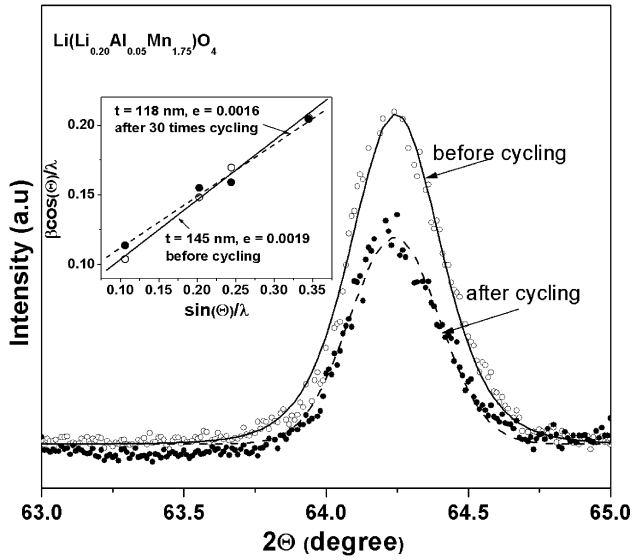

Fig. 9. The experimental (symbol) and fitted (line) slow scanned XRD plot of (4 4 0) diffraction peak of lithium and aluminum ion co-doped lithium manganate before and after cycling. The inset shows the linear fit of $\beta \cos\theta/\lambda$ vs. $\sin\theta/\lambda$ plot to calculate the crystallite size (from intercept) and lattice strain (from slope) before and after cycling (see text).

cathode before and after electrochemical cycling. The inset shows the linear $\beta \cos\theta/\lambda$ versus $\sin\theta/\lambda$ plot. The calculated lattice parameter before and after cycling remains $\sim$8.18×. The crystallite site and lattice strain are marginally reduced after cycling. All these results are supportive to the fact that Mn^{3+} ion contents after charge–discharge cycling are significantly reduced in co-doped cathode, and therefore, the onset of J–T distortion is delayed further at least up to the cut-off voltage $\sim$3.4.

Fig. 10 shows that as predicted, the cycleability is indeed improved appreciably in co-doped LMO cathode due to the delayed onset of J–T distortion. The capacity repeated

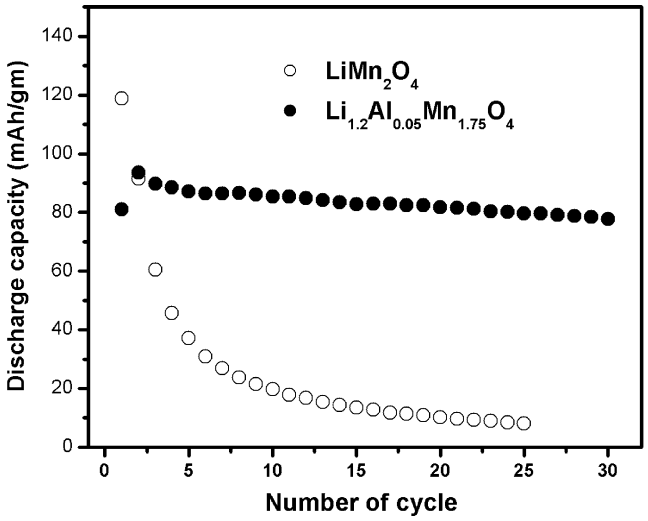

Fig. 10. Comparison of the cycleability behavior of pure and Li and Al ion co-doped lithium manganate composite cathodes.

cycling remains always higher than the theoretical prediction even after. Taking the capacity of co-doped material $\sim$75 mAh/g, it can be calculated back that 0.47 M Li is actually participating in the electrochemical reaction and Mn valence state at the top of the charge is +4.06. Although the valence state of Mn^{+} more than +4 is possible, further studies are required to clarify these issues.

4. Conclusions

We have successfully synthesized nano-crystalline (diameter < 100 nm) lithium manganate (LMO) particles by an acetate based chemical solution route. In the 4.2–3.4 V range at 0.98 C discharge rate, the capacity of nano-crystalline LMO was 120 mAh/g. However, even in the 4 V ranges, severe capacity fading was observed when these cathodes were cycled at constant current of 0.98 C. By analyzing the slow scanned X-ray diffractograms of as prepared and cycled composite cathodes, we found that both the lattice strain as well as crystallite size of LMO particles were increased after the charge–discharge cycling. The XPS analysis in conjunction with the micro-Raman spectroscopy indicated that at the surface of LMO particles, the Mn^{3+} ion contents were increased after charge–discharge cycling. The increase of Mn^{3+} ion contents as well as lattice strain could be related with the formation of tetragonal $Li_2Mn_2O_4$ type compound at the surface of LMO particles having otherwise cubic spinel structure. The reason for the severe capacity fading of nano-crystalline LMO powders were believed to be due to the onset of the Jahn–Teller distortion towards the end of the discharge. By simultaneous Li and Al doping (replacing Mn in the octahedral 16d site), the average oxidation state of Mn ions in virgin LMO electrodes was increased and thereby the onset of cubic to tetragonal structural transition (Jahn–Teller) was delayed. Although the discharge capacity of these co-cation doped lithium manganate was reduced, but their cycleability was dramatically improved. The doping contents of Al and Li are needed to be further optimized to increase the discharge capacity of these nano-crystalline cathode materials.

Acknowledgements

The above research work was partially supported by the research grants from DoE (#DE-FG02-01ER45868) and NASA (#NAG3-2676) Glenn research center. XPS measurements were carried out utilizing the facilities at the Materials Characterizing Center (MCC).

References

[1] J.J. Xu, G. Jain, Electrochem. Solid State Lett. 6 (2003) A190.
[2] P. Poizot, S. Laruelle, S. Grugeon, L. Dupont, J.M. Tarascon, Nature 407 (2000) 496.

[3] H. Li, X. Huang, L. Chen, Z. Wu, Y. Liang, Electrochem. Solid State Lett. 2 (1999) 547.
[4] G. Maurin, F. Henn, B. Simon, J.F. Colomer, J.B. Nagy, Nano Lett. 1 (2001) 751;
I. Mukhopadhyay, N. Hoshino, S. Kawasaki, F. Okino, W.K. Hsu, H. Touhara, J. Electrochem. Soc. 149 (2002) A39.
[5] S. Passerini, F. Coustier, M. Giorgetti, W.H. Smyrl, Li–Mn–O aerogels, Electrochem. Solid State Lett. 2 (1999) 483.
[6] N. Li, C.J. Patrissi, G. Che, C.R. Martin, J. Electrochem. Soc. 147 (2000) 2044;
C.R. Sides, N. Li, C.J. Patrissi, B. Scrosati, C.R. Martin, Mater. Res. Soc. Bull. (August) (2002) 604.
[7] J.B. Bates, N.J. dudney, B. Neudecker, A. Ueda, C.D. Evans, Solid State Ionics 135 (2000) 33.
[8] F. Croce, G.B. Appetecchi, L. Persi, B. Scrosati, Nature 394 (1998) 456.
[9] Y. Shin, A. Manthiram, J. Electrochem. Soc. 151 (2004) A204.
[10] A. Hagfeldt, N. Vlachopoulos, M. Gratzel, J. Electrochem. Soc. 141 (1994) L82.
[11] C.J. Curtis, J. Wang, D.L. Schulz, J. Electrochem. Soc. 151 (2004) A590.
[12] Y. Shin, A. Manthiram, J. Power Sources 126 (2004) 169.
[13] A. Odani, A. Nimberger, B. Markovsky, E. Sominski, E. Levi, V. G Kumar, M. Motiei, A. Gedanken, P. Dan, D. Aurbach, J. Power Sources 119–121 (2003) 517.
[14] J.S. Kim, J.T. Vaughey, C.S. Johnson, M.M. Thackeray, J. Electrochem Soc. 150 (2003) A1498.
[15] H.J. Choi, K.M. Lee, G.H. Kim, J.G. Lee, J. Am. Ceram. Soc. 147 (2001) 242.
[16] P. Lucas, C.A. Angell, J. Electrochem. Soc. 147 (2000) 4459.
[17] S.H. Kang, J.B. Goodenough, L.K. Rabenberg, Electrochem. Solid State Lett. 4 (2001) A49.
[18] N. Santander, S.R. Das, S.B. Majumder, R.S. Katiyar, Surf. Coat. Technol. 177–178 (2004) 60.
[19] G.K. Williamson, W.H. Hall, Acta Metall. 1 (1953) 222.
[20] J.B. Goodenough, M.M. Thackeray, W.I.F. David, P.G. Bruce, Rev. Chim. Miner. 21 (1984) 435.
[21] H. Bjork, T. Gustafsson, J.O. Thomas, Electrochem. Commun. 3 (2001) 187.
[22] M.M. Thackeray, A. de Kock, M.H. Rossouw, D. Liles, R. Bittihu, D. Hodge, J. Electrochem. Soc. 139 (1992) 363.
[23] B.D. Cullity, Elements of X-Ray Diffraction, Addison–Wesley, New York, 1978, p. 281.
[24] T. Eriksson, T. Gustafsson, J.O. Thomas, Electrochem. Solid State Lett. 5 (2002) A35.
[25] B. Ammundsen, G.R. Burns, M.S. Islam, H. Kanoh, J. Roziere, J. Phys. Chem. B 103 (1999) 5175.
[26] H.T. Chung, S.T. Myung, T.H. Cho, J.T. Son, J. Power Sources 97 (2001) 454.
[27] Y. Xia, Y. Zhou, M. Yoshio, J. Electrochem. Soc. 144 (1997) 2593.
[28] D.H. Jang, Y.J. Shin, S.M. Oh, J. Electrochem. Soc. 143 (1996) 2204.
[29] H. Yamane, T. Inoue, M. Fujita, M. Sano, J. Power Sources 110 (2002) 19.
[30] T. Inoue, M. Sano, J. Electrochem. Soc. 145 (1998) 3704.
[31] A.Du. Pasquier, A. Blyr, P. Courjal, D. Larcher, G. Amatucci, B. Gerand, J.M. Tarascon, J. Electrochem. Soc. 146 (1999) 428.
[32] R.J. Gummow, A. de Kock, M.M. Thackeray, Solid State Ionics 69 (1994) 59.
[33] M.M. Thackeray, Y.S. Horn, A.J. Kahajan, K.D. Kepler, E. Skinnev, J.T. Vaughey, S.A. Hackney, Electrochem. Solid State Lett. 1 (1998) 7.
[34] Y. Shin, A. Manthiram, Electrochem. Solid State Lett. 5 (2002) 55.
[35] J.C. Hunter, J. Solid State Chem. 39 (1981) 142.
[36] M.M. Thackeray, J. Am. Ceram. Soc. 82 (1999) 3347.
[37] R.V. Chebian, A.M. Kannan, F. Prado, A. Manthiram, Electrochem. Commun. 3 (2001) 624.